Cronfa - Swansea University Open Access Repository

_____

This is an author produced version of a paper published in:
Journal of Geophysical Research: Earth Surface

_____

Cronfa URL for this paper:

_____

Paper:

http://www.swansea.ac.uk/iss/researchsupport/cronfa-support/

Ice and firn heterogeneity within Larsen C Ice Shelf from borehole optical televiewing

David W. Ashmore[1], Bryn Hubbard[1], Adrian Luckman[2], Bernd Kulessa[2], Suzanne Bevan[2], Adam Booth[3], Peter Kuipers Munneke[4], Martin O'Leary[2], Heidi Sevestre[5] and Paul R. Holland[6]

1 – Centre for Glaciology, Department of Geography and Earth Sciences, Aberystwyth University, SY23 3DB, UK;

2 – Geography Department, College of Science, Swansea University, SA2 8PP, UK;

3 – School of Earth and Environment, University of Leeds, Leeds, LS2 9JT, UK, ;

4 – IMAU, Utrecht University, P.O. Box 80000, 3508 TA Utrecht, The Netherlands;

5 – School of Geography and Geosciences, University of St. Andrews, College Gate, St. Andrews, Fife, KY16 9AJ, UK

6 – British Antarctic Survey, High Cross, Madingley Road, Cambridge, CB0ET

Corresponding author: David Ashmore (david.w.ashmore@outlook.com)

Key Points

- **Larsen C Ice Shelf is composed of distinct material facies units recording its dynamic and melt history**
- **Existing firn air estimates commonly neglect the presence of buried low-density continental ice**
- **>40% of the firn zone of Larsen C is composed of refrozen ice in its central and northern sectors**

Abstract

We use borehole optical televiewing (OPTV) to explore the internal structure of Larsen C Ice Shelf (LCIS). We report a suite of five ~90 m long OPTV borehole logs, recording a LED-illuminated geometrically-correct image of the borehole wall, from the northern and central portions of LCIS collected during austral spring 2014 and 2015. We use a thresholding-based technique to estimate the refrozen ice content of the borehole column and exploit a recently calibrated density—luminosity relationship to reveal the structure of each site in detail. All sites are dense and strongly influenced by surface melt, with frequent refrozen ice layers and mean densities 1.87-90 m ranging from 862 to 894 kg m^{-3}. We define five distinct material facies that comprise LCIS and relate these to ice provenance, dynamic history and past melt events. These facies are *in situ* meteoric ice (F1), ice that has undergone enhanced densification (F2), refrozen melt pond ice (F3), compressed F2/F3 ice (F4), and advected continental ice (F5). We show that the OPTV-derived pattern of firn air content is consistent with previous estimates, but that a significant proportion of firn air is contained within our F5 unit, that we interpret to be deposited inland of the grounding line. The structure of LCIS is strongly influenced by the E-W gradient in föhn-driven melting with sites close to the Antarctic Peninsula being predominantly comprised of refrozen ice. Melting is also substantial towards the ice shelf centre with >40% of the firn zone overall being comprised of refrozen ice.

1. Introduction

Ice shelves fringe much of Antarctica and are particularly sensitive indicators of environmental changes owing to their low elevation, lower latitude and exposure to both oceanic and atmospheric forcing. Ice shelves form when glaciers and ice streams flowing across the grounding line begin to float and spread laterally to fill an embayment. Once established by this core of continental ice, they are able to gain and lose mass at their upper and lower interfaces, as well as calving at the marine margin. Although ice shelves are floating, and therefore experience negligible basal shear stress, lateral stresses and intermittent pinning to the seabed result in an ability to buttress grounded ice upstream. Through this, ice shelves modulate the contribution of the Antarctic Ice Sheet to eustatic sea level rise. Where ice shelves have thinned or collapsed inflowing glaciers are observed to have accelerated and their discharge to have increased accordingly (e.g. Paolo et al., 2015; De Rydt et al., 2015; Scambos et al., 2004).

A critical characteristic of ice shelves is their predisposition to lose mass episodically once their geometry becomes unstable (Kulessa et al., 2014). The end-member of this behaviour is a near-total disintegration of ice shelves, best exemplified by the collapse of Larsen B Ice Shelf in early 2002 (Scambos et al., 2003). The disintegration of Antarctic Peninsula ice shelves has progressed poleward for the last 30 years commensurate with climate warming (Cook and Vaughan, 2010) and a mean annual isotherm of -9 °C has been proposed as a practical limit of viability for ice shelves (Morris and Vaughan., 2003). The largest remaining Antarctic Peninsula ice shelf, Larsen C Ice Shelf (LCIS), is intersected by this isotherm and may be currently experiencing surface melting conditions similar to those that preceded the collapse of its neighbours, Larsen A in 1995 and Larsen B in 2002. The surface of LCIS has lowered during the satellite era, and approximately half of this lowering signal is caused by the loss of air from the ice shelf firn (Holland et al., 2015). This air loss may be related to

66 decreased surface accumulation or enchanced melting or firn compaction associated with the

67 historical warming of the Antarctic Peninsula (Turner et al., 2016).

68 Proposed mechanisms of ice shelf disintegration commonly invoke intense surface melting

69 and ponding leading to flexure and (hydro-) fracture (Banwell et al., 2013; Scambos et al.,

70 2009). In order for melt ponds to form, snowpack pore space must be first filled (Kuipers

71 Munneke et al., 2014) or a layer of impermeable refrozen (infiltration) ice of sufficiently

72 large thickness and extent must exist (e.g. Machguth et al., 2016).

73 Distributed estimates of ice shelf thickness, a fundamental input into glaciological models,

74 are typically derived through satellite altimetry by way of an assumption of hydrostatic

75 equilibrium, requiring a correction for the low-density firn layer. Modelling (Pritchard et al.,

76 2012; Chuter and Bamber, 2015) and geophysical (Drews et al., 2016) methods typically

77 prescribe a shape to the depth-density profile. However, recent results show that intense

78 surface melt in one NW inlet on LCIS has led to an anomalously dense ~42 m thick layer of

79 refrozen ice and an irregular density profile over the upper 97 m (Hubbard et al., 2016). Here,

80 the firn zone is ~10 °C warmer and ~170 kg m^{-3} denser than would be expected without melt

81 pond refreezing. The presence of this rheologically softer ice has implications for

82 understanding and predicting ice shelf flow and fracture in warming regions. The stability of

83 ice shelves also depends therefore on their large-scale three-dimensional structural

84 composition and stress field. Surface mapping (Glasser et al., 2009) and ground-penetrating

85 radar surveys (McGrath et al., 2014) show evidence of suture ice down-flow of coastal

86 promontories and islands. This warmer, softer ice (Dierckx et al., 2012) is thought to form by

87 the basal freeze-on of seawater in the lee of flow obstacles and appears farther down-flow to

88 hinder the large-scale transverse propagation of brittle fractures such as basal crevasses

89 (McGrath et al., 2012) and rifts (Jansen et al., 2015; Kulessa et al., 2014).

90   The requirement for knowledge of the three-dimensional structure of ice shelves places a

91   reliance on inferences from geophysical data or labour-intensive ice core drilling. Borehole

92   hot-water drilling and optical televiewing (OPTV) is able to make a contribution to this

93   requirement by being relatively rapid and logistically undemanding and, as a direct RGB

94   image of the borehole wall is acquired, highly complementary to surface- or airborne

95   geophysical surveys. The aim of this paper is to investigate LCIS internal structure. Herein

96   we present five borehole OPTV records, including the one presented and discussed briefly by

97   Hubbard et al. (2016), thereby enabling spatially-distributed ice facies fields to be considered

98   in detail across the northern and central portions of the ice shelf.

2. Field site and data

LCIS covers an area ~50,000 km^2 on the eastern Antarctic Peninsula (Fig. 1). Föhn winds in the lee of the Graham Land mountains (Elvidge et al., 2015) intermittently deliver warm air to the shelf, driving intense surface melt which occasionally forms melt ponds visible in SAR imagery (Holland et al., 2011; Luckman et al., 2014). Analysis of weather stations located in the remnant Larsen B area indicates that, at least that region, has experienced föhn events of increased frequency and temperature over the last ~50 years, likely driven by a positive trend in the Southern Annular Mode (Cape et al., 2015). Airborne radar estimates of bulk firn air content, the equivalent reduction in ice thickness if it were completely comprised of bubble-free glacial ice, indicate a near-complete depletion of firn air in the NW inlets, with firn air increasing eastwards and southwards (Holland et al., 2011). Repeated radar surveys along a transect through the centre of LCIS show a loss of firn air averaging ~4 cm yr^{-1} during 1998-2012 (Holland et al., 2015).
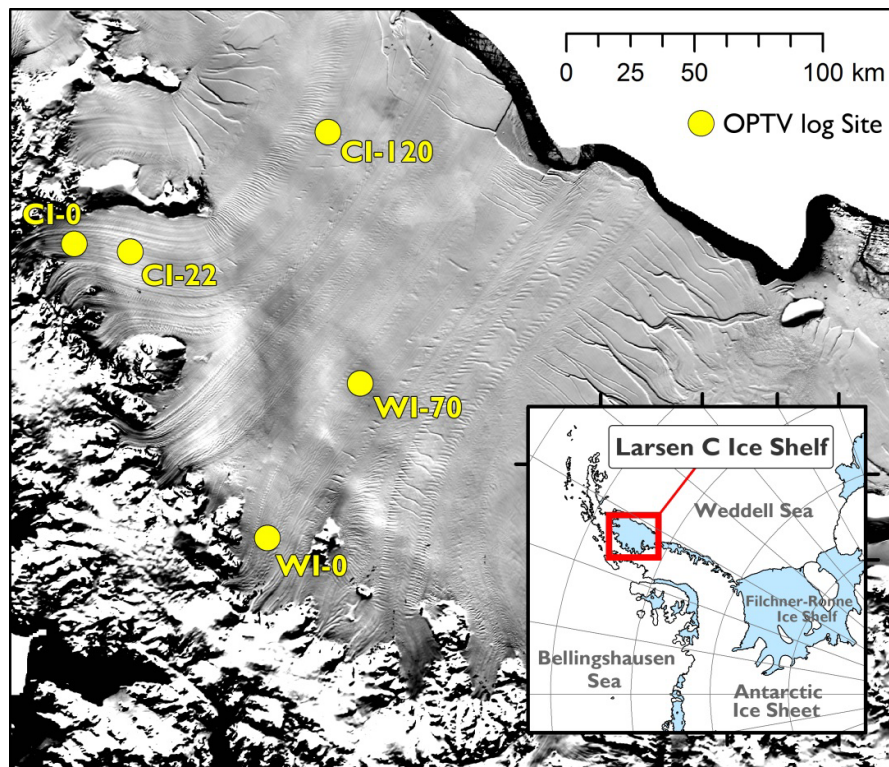
Figure 1. Location map of LCIS showing the sites of OPTV borehole logs overlain on 2009

114   *MODIS "MOA" image.*

115   Study sites were selected in order to sample the evolution in ice properties along both N-S

116   and E-W gradients. Three drill sites lie on a flowline emanating from Cabinet Inlet (CI)

117   spaced at 0, 22 and 120 km, and two further drill sites lie on a flowline emanating from

118   Whirlwind Inlet (WI) spaced at 0 and 70 m along flow (Fig. 1). Boreholes are named

119   according to their associated inlet and along-flow distance (see Fig. 1). CI-0, CI-22 and WI-0

120   are considered as "inlet sites" and CI-120 and WI-70 as "shelf sites." CI-0, presented by

121   Hubbard et al. (2016), was drilled in November 2014 and the remaining four boreholes

122   drilled in November and December 2015. All OPTV logs begin at 1.87 m depth, the length of

123   the OPTV sonde, and reach depths of 90 or 97.5 m (Table 1).

124   *Table 1. Site locations and depths.*

Site	Start (m)	Depth (m)	Location
CI-0	1.87	97.5	-66.403 -63.377
CI-22	1.87	90	-66.588 -63.212
CI-120	1.87	90	-67.001 -61.486
WI-0	1.87	90	-67.444 -64.953
WI-70	1.87	90	-67.500 -63.336

125

126

127   3. **Methods**

128   *3.1. Hot-water drilling and optical televiewing*

129   Drilling used pressurised hot water, resulting in boreholes of ~12 cm diameter. The ice

130   column stratigraphy was logged using an optical televiewer (OPTV) instrument. This

131   technique has previously been described in detail by Hubbard et al. (2008). The borehole wall

132   is illuminated by a ring of 72 sonde-mounted LEDs while a downward-looking CCD camera

133   records a reflected image on a hyperboloidal mirror. This results in a geometrically accurate

134   RGB image of the complete borehole wall which can be rolled and visualised as a 3D "virtual

135   core". As the borehole is solely illuminated by stable sonde-mounted LEDs, image brightness

136   is a measure of borehole wall reflectivity. Elsewhere in Antarctica, OPTV has been used

137   successfully in boreholes to identify facies associated with a rift on Roi Baudouin Ice Shelf,

138   including the identification of marine ice and infiltration ice layers (Hubbard et al., 2012).

139   The OPTV image resolution is defined during acquisition and a balance must be struck as

140   higher resolution necessitates a reduction in the logging rate. For our images we sample 360

141   pixels in each row and sample the borehole vertically every 1 mm. The exception to this is

142   CI-22 where a 2 mm vertical sampling rate was used due to inclement weather conditions

143   during acquisition.

144   *3.2. Density derivation*

145   Borehole image brightness, averaged by row, commonly referred to as luminosity has been

146   shown to be a good proxy for firn and ice density on metre scales (Hubbard et al., 2013). The

147   underlying principle being that borehole reflectance decreases with density under a stable

148   light source. Density (ρ) is reconstructed from the equation:

$$\rho = 950 - 40e^{(0.0101L)} , \qquad\qquad [1]$$

149   where *L* is borehole luminosity (Malone et al., 2013) following Hubbard et al. (2016).

150   Slight coaxial misalignment of the OPTV sonde and irregularities in the borehole shape, most

151   notably by drill hose incision into soft snow and firn of the upper sections of CI-22 and WI-

152   70, result in occasional anomalously dark regions of some OPTV sections. This effect is

153   caused by the narrow, incised notch being improperly illuminated and appearing as a quasi-

154   vertical "shadow" on the complete OPTV log. To minimise this effect on our estimated

155   density profiles we reject the upper and lower quartile brightness values on each row when

156   calculating luminosity. Across all logs the mean difference between filtered and unfiltered

157   density is -0.066 ± 3.30 kg m^{-3}. In the upper part (1-30 m) of WI-70, where hose incision is

158   most apparent the mean difference is -1.15 ± 2.50 kg m^{-3}. Firn air volume fraction (ϕ) is

159   calculated for each depth bin from the OPTV derived density (ρ) where the density of glacial

160   ice is taken as ρ_i = 917 kg m^{-3} by:

$$\phi = 1 - \frac{\rho}{\rho_i} \qquad\qquad [2].$$

161   To estimate firn air content of the upper 1.87 m, which is not televiewed due to the length of

162   the sonde, we use 0.6 m deep snow pits at CI-0, CI-60 (i.e. 60 km along flowline) and CI-

163   120. Here density was measured gravimetrically using a cylindrical cutter (see Proksch et al.,

164   2016) at 0.05 m increments yielding a mean density of 357 ± 8.8 kg m^{-3}. We then assume a

165   linear increase in density from this value to the mean OPTV-derived density in the upper 0.1

166   m of the OPTV log and add this to our OPTV-derived firn air thickness.

167   *3.3. Facies analysis*

168   Ice character is a function of (1) surface conditions at and shortly after deposition and (2) post

169   burial compaction-metamorphism and deformation. The principle adopted here is that spatio-

170   temporal differences in these processes lead to classifiable ice facies. Our approach is to

171 describe facies based on layer style, density characteristics and depth without assigning a

172 genetic mechanism. These can then be interpreted subsequently in terms of physical

173 processes and environments. While some environments lead to distinct facies contrasts (e.g.

174 Hubbard et al., 2012) others lie upon a spectrum where the effect of a particular process

175 becomes increasingly dominant. In such cases the division between facies is made in a

176 consistent, reproducible manner. We achieve this by exploiting the situation whereby the

177 principal characteristic of the facies we report is the contrast between the host ice and

178 included layers. To quantify this we define, σ_ρ, the standard deviation of density over a 2 m

179 moving window with depth. This practical definition is adopted as 2 m represents a distance

180 that likely contains several years of accumulation but one which is not strongly influenced by

181 the decrease in brightness associated with densification due to burial. Thresholds of σ_ρ can

182 then be stipulated in response to potentially ambiguous facies boundaries.

183 *3.4. Image thresholding and infiltration ice estimation*

184 Three principal processes affect the stratigraphy of ice shelves. The accumulation of snow

185 may result quasi-regular surface-parallel layering reflecting depositional differences during

186 accumulation, often referred to as primary stratification in structural glaciology (Hudleston,

187 2015). Second, the snowpack undergoes depth-related densification by compaction-

188 metamorphism driven by snow temperature and the weight of the overlying snow. Third,

189 surface meltwater that percolates into a cold snowpack refreezes to form bubble-poor, dense

190 infiltration ice, identifiable as dark (low reflectance) layers in OPTV logs. Furthermore, ice

191 inherited from inland may also be overprinted during a variety of brittle and ductile

192 deformation processes relating to dynamic flow, for example, by the incorporation of debris

193 (Glasser et al., 2014) or platelet ice of marine origin (Hubbard et al., 2012).

194   Primary stratification in our LCIS logs is typically faint and disrupted by melt processes (see

195   Section 4.1), so we can consider OPTV images to chiefly comprise of infiltration ice layers

196   overprinted onto a densifying host ice. The resulting bimodal distribution of pixel

197   brightnesses lends itself well to image thresholding analysis (e.g. Kinnard et al., 2008) which

198   allows the consistent and reproducible identification of infiltration ice layers. It is important,

199   however, to consider the main ice facies when interpreting thresholding results. Where ice is

200   relatively homogenous other features, which may arise from trapped bubbles, incorporated

201   debris or healed fractures may be identified by the algorithm. In this case the threshold-

202   identified layers do not coincide with refrozen ice layers.

203   Uneven illumination is a well-known issue in the successful application of thresholding

204   algorithms. Here, we prepare our OPTV logs prior to thresholding in order to minimise lateral

205   and vertical biases in image brightnesses not related to glaciological features and maximise

206   the effectiveness of image thresholding. Areas of anomalous illumination are removed by

207   row (Section 3.2) and images were smoothed with a 1x10 pixel wide median filter to

208   highlight vertical gradients in brightness. Images were detrended with a sum-of-sine function

209   fitted to the luminosity profile in order to remove long-wavelength density variations with

210   depth (Fig. 2). Thresholding was then performed sequentially on 2 m image sections to

211   achieve optimal results as some minor long-wavelength variations in image brightness remain

212   with depth even after detrending. Three common auto-thresholding algorithms were tested by

213   trial and error: those of Ridler and Calvard (1978), Kittler and Illingworth (1986), and Otsu

214   (1979). Otsu's (1979) method performed most consistently and was adopted for this

215   investigation.

216   Otsu's (1979) auto-thresholding technique divides a given distribution's population into two

217   clusters based on a threshold value and calculates the difference between these clusters. The

218   optimal threshold is arrived at by finding the values at which the maximum difference

219   between these clusters is attained. The result is a binary image in which each pixel is

220   classified as either low or high brightness. For our application herein, any pixel row classified

221   as over 90% "low brightness" is identified as "dark" (Fig. 2), allowing OPTV images to be

222   characterised in terms of their thresholding output percentage.
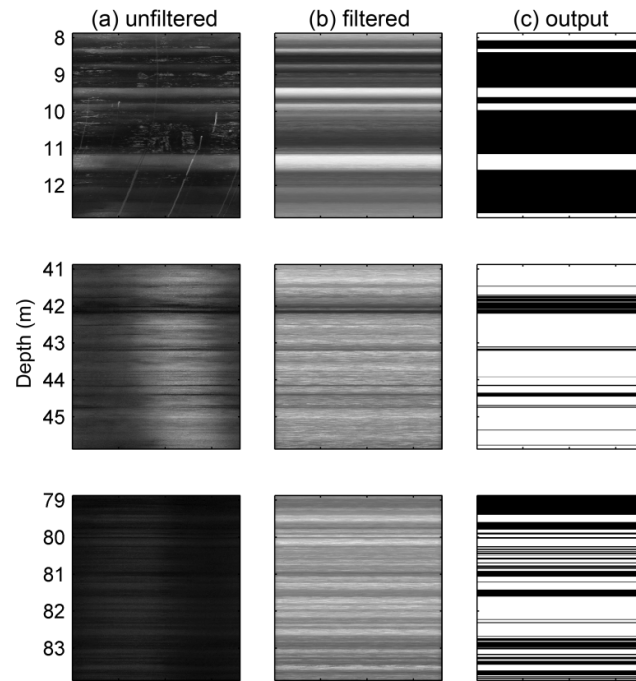
223

224   *Figure 2. Stages of thresholding as applied to three environments (figure rows) from the CI-*

225   *120 OPTV borehole log. Columns show: (a) Raw OPTV log; (b) The result of the rejection of*

226   *upper and lower quartile values by row, vertical detrending and the application of the*

227   *median filter; and (c) The result of thresholding to reveal the "dark" layer population.*

228

4. Results

4.1. Optical televiewing and density profiles

Optical televiewer logs and the derived density profiles from the northerly Cabinet Inlet flowline are presented in Fig. 3 and those from the southerly Whirlwind Inlet in Fig. 4. Borehole logging reveals the presence of layers and distinct units across all five sites with several logs displaying clear, visually identifiable step changes in style (explored further in Section 4.2). The ice column of LCIS varies in both N-S and E-W directions in terms of layer presence, layer style, contrast between layers and host ice, and the decrease in host ice brightness with depth. Bright host ice is increasingly present in the easterly (seaward) and southerly directions, particularly in the upper part of the logs, while dark, homogenous ice is increasingly present in the westerly (inland) and northerly directions. All the LCIS logs contrast strongly with OPTV logs from other polar ice masses, including Derwael Ice Rise and Roi Baudouin Ice Shelf, East Antarctica (Hubbard et al., 2013) and Summit, Greenland (Hubbard and Malone, 2013). In these logs images darken gradually with depth, discrete dark layers are infrequent and faint regular banding is commonly visible. Such features are entirely absent from the LCIS results presented here.

The mean density from all our sites is 873.1 ± 39.2 kg m-3, denser and less variable than Roi Baudouin Ice Shelf where mean OPTV-derived density $1.87 – 66.1$ m is 742.4 ± 86.8 kg m^{-3} (Hubbard et al., 2013). The spatial variation in firn/ice column identified visually is reflected in the luminosity-derived density results (summarised in Table 2). They demonstrate that CI-22 has the highest mean density, while WI-70 has the lowest mean density, although only separated by 32.6 kg m^{-3}. Density standard deviation indicates that CI-22 has the least variable ice and firn column while WI-70 has the most variable profile. Firn air content estimates affirm this spatial pattern as they are directly calculated from density. With the

253   exception of CI-0, a picture emerges of the large-scale density characteristics of LCIS, where

254   the densest ice is centred towards the north and inland portions, with the ice shelf becoming

255   progressively less dense towards the south and the calving margin. CI-0 and WI-0 both host a

256   density inversion at ~45 m and ~65 m depth respectively (Table 3). Using a 2 m moving

257   average of density we estimate the depth to the pore closure density of 830 kg m^{-3} (Table 2),

258   this is important as it represents in the maximum depth percolating meltwater can possibly

259   reach before refreezing. Despite the lower mean density of CI-0 the pore closure depths from

260   all sites conform to the W-E and N-S pattern, due to the thick layer of impermeable pond ice

261   at 2.9 m depth, as noted by Hubbard et al. (2016).

262   *Table 2. Summary of density characteristics from LCIS boreholes. Mean density and firn air*

263   *are calculated over the common depth range of 1.87-90.00 m for all logs and 1.87–97.50 m*

264   *for CI-0 (parenthesised). Surface corrected firn air content refers to the firn air content with*

265   *the firn air contained within the upper 1.87 m added. Pore close off density is taken as 830 kg*

266   *m^{-3} and determined with a 2 m moving average of the density profile.*

Site	Depth mean density (± 1σ) (kg m^{-3})	Firn air content (m)	Firn air content (surface corrected, m)	Pore closure depth (m)
CI-0	872.2 ± 30.4 (868.3 ± 32.0)	4.31 (5.08)	5.18 (5.95)	3.29
CI-22	894.2 ± 21.8	2.20	2.87	4.18
CI-120	879.0 ± 27.7	3.65	4.46	6.05
WI-0	873.2 ± 42.7	4.21	4.99	7.67
WI-70	861.6 ± 51.8	5.32	6.18	8.43

267

268
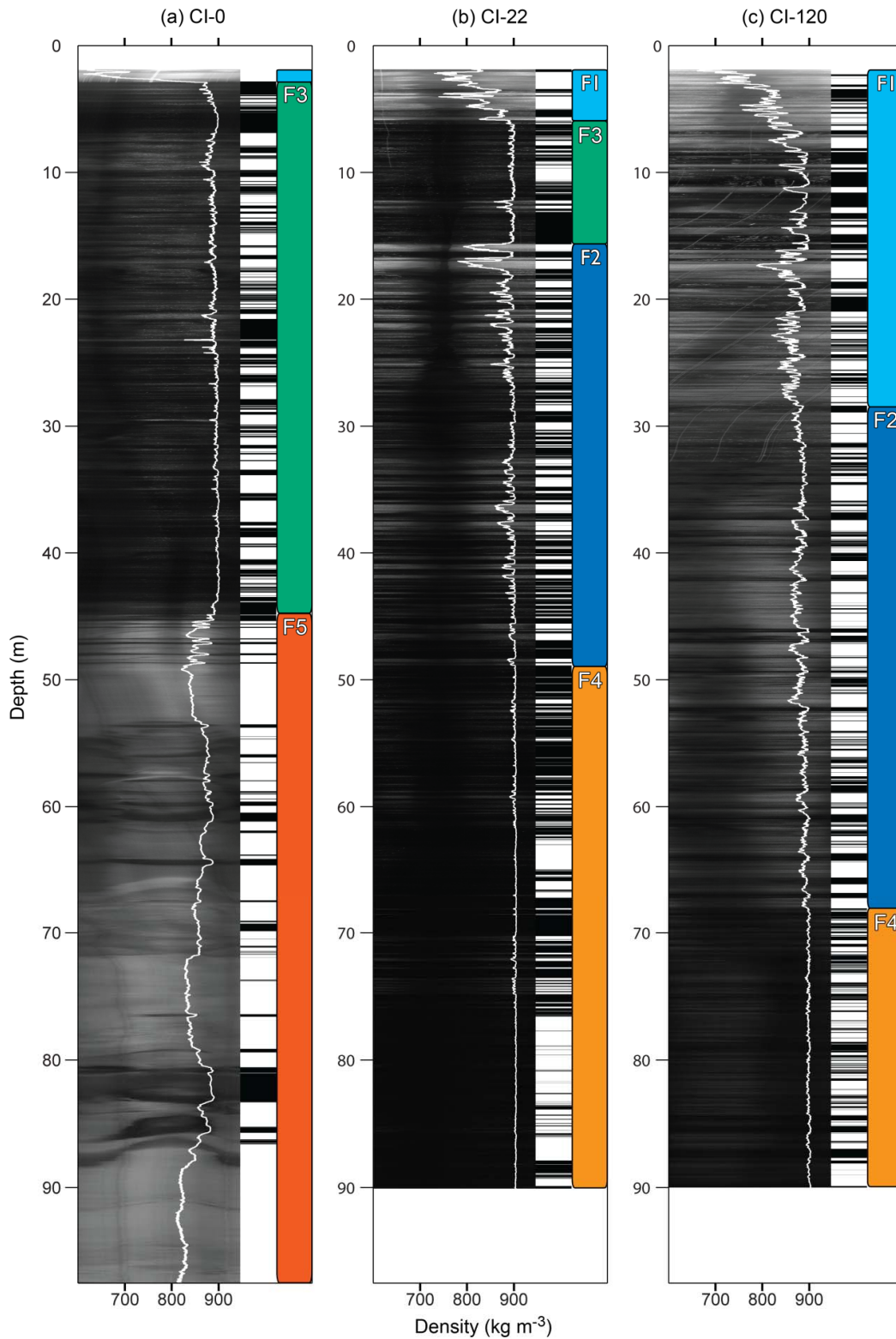
Figure 3. Borehole OPTV raw log and density profile (left), binary thresholding output (middle) and facies classification (right) results from (a) CI-0, (b) CI-22 and (c) CI-120.
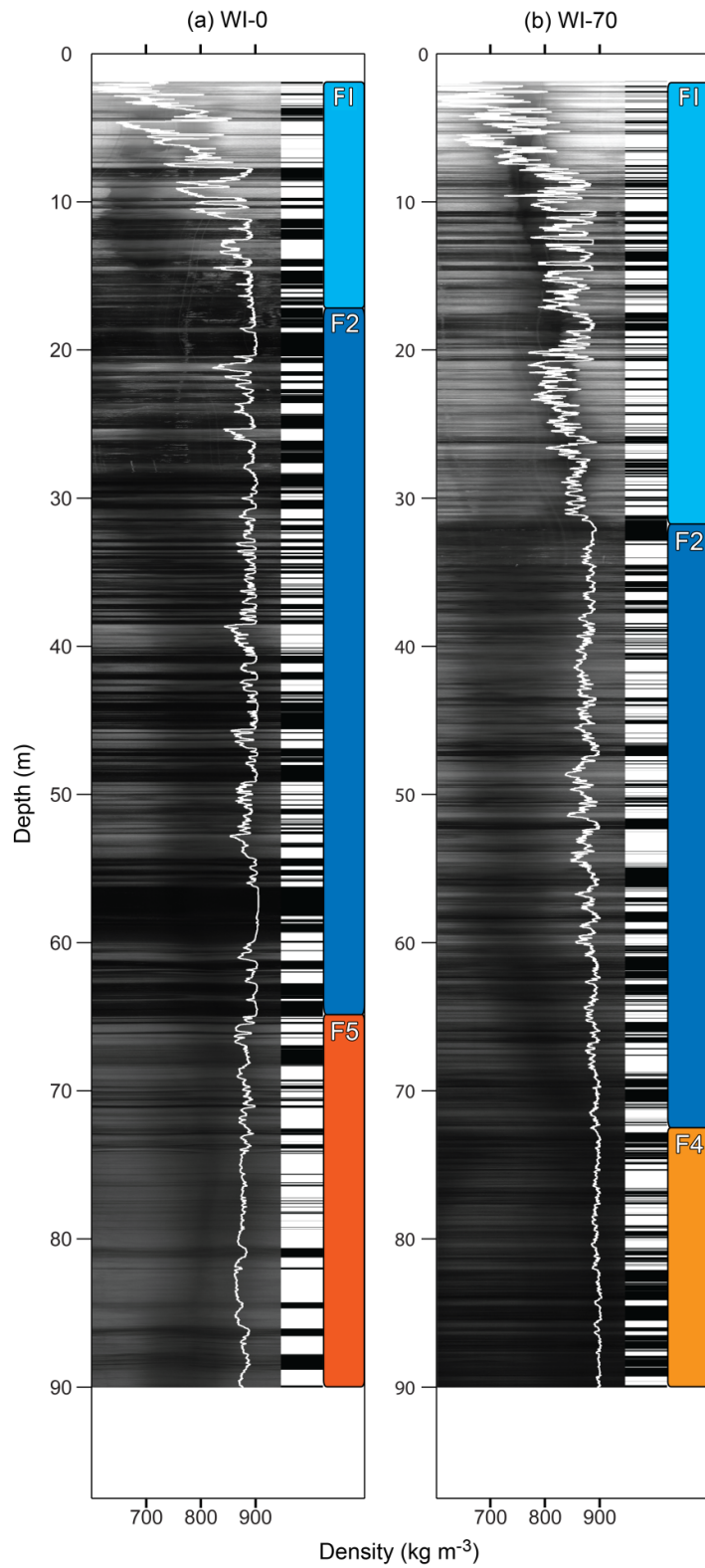
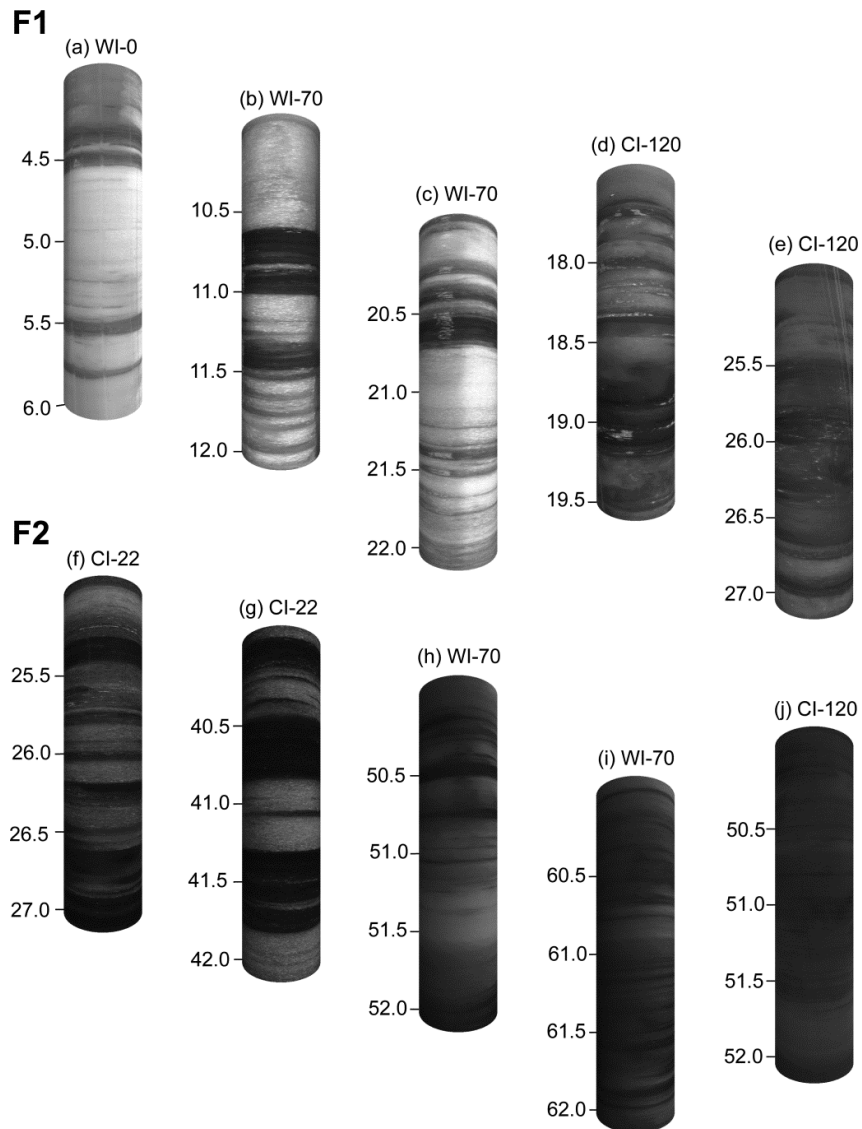Figure 4. Borehole OPTV raw log and density profile (left), binary thresholding output (middle) and facies classification (right) results from (a) WI-0 and (b) WI-70.

275   *4.2. Facies classification*

276   Five facies are defined on the basis of characteristics revealed by the OPTV logs (Fig. 5-7),

277   named F1-F5 with increasing number broadly referring to increasing depth within the ice

278   column, although not all facies are present at all sites. The distribution of facies with depth is

279   presented in Fig. 3 (Cabinet Inlet flowline) and Fig. 4 (Whirlwind Inlet flowline), and

280   summarised in Table 3.

281   F1 is present in all logs as the uppermost unit and is characterised by depth-darkening host

282   material over metre scales and as containing frequent dark layers which may be centimetres

283   to decimetres thick (Fig. 5a-e). The brightness of dark layers decreases also with depth, for

284   example, Fig. 5a shows clearly identifiable dark layers, but they are not as prominent as those

285   in Fig. 5b or 5d. Host ice darkening rates are site-specific, such that despite occurring at a

286   shallower depth CI-120, 17.5-19.5 m is visibly darker than WI-70 20 – 22 m (cf. Fig. 5d and

287   5c). We note that F1 is a dynamic environment in which melt and densification are ongoing

288   at significant levels. With this, we note that the CI-0 log was collected in Nov 2014, whereas

289   all others were acquired in Nov/Dec 2015 and that melt ponds were visible in Cabinet Inlet in

290   March 2015.

291   F2 contains bright host ice and dark layers some centimetre or decimetres thick (Figs. f-j), but

292   the density contrast between host ice and layers is much reduced relative to F1 (Figs. 3 and

293   4). F2 host material is variable but not darkening on the metre scale with depth. Fig. 5e

294   demonstrates the difficulty in qualitatively defining facies boundaries and thus we define the

295   F1-F2 transition as the shallowest point σ_ρ (Section 3.3) decreases below a threshold of 5 kg

296   m^{-3}. This value represents the start of a new regime although σ_ρ may exceed this value deeper

297   in the log due to occasional bright firn layers (Fig. 5g). The F1/F2 boundary may be visually

298   striking, as in WI-70, or gradual, as in CI-120.

Figure 5. Rolled virtual core images of LCIS borehole OPTV logs arranged by depth (not to scale) of F1 and F2 with actual depth given in metres.

F3 is dark without defined layers as present in F1/F2 (Fig 6a-g). However, structure is visible by bright speckles that form clouds, layers and, in one case, vertical streaking structures (Fig. 6a and 6g). Layers are typically diffuse and faint (Fig. 6b and 6e) but can be well defined (Fig. 6c). F3 is present only in CI-0 and CI-22, forming units of 41.57 and 9.74 m thick respectively. The upper transition into F3 is abrupt and the base of F3 units is moderately abrupt and followed by a reappearance of dark layers (Fig 6f and 7a).

308   F4 occurs exclusively beneath F2 and is characterised by a decrease in contrast between host

309   material and layers due to darkening of the normally bright host material. Structure remains

310   visible in some F4 sections (Figs 6h, 6j and 6k) as relatively dark layers overprinted on a

311   lighter host material similar to those in F1 and F2. However, structure within F4 is less clear

312   deeper in CI-22 (Fig. 6i) where it appears near-uniformly dark and homogenous. These

313   sections without visible structure are characterised by occasional bright speckles similar to

314   those in F3 (Fig. 6i). The F2/F4 transition is also variable and may be relatively abrupt as in

315   CI-120 (Fig. 3c), moderately abrupt as in CI-22 (Fig 3b), or gradual as in WI-70 (Fig. 4b).

316   Therefore we use σ_ρ in an effort to define this facies boundary consistently, adopting the

317   working definition that the F2/F4 transition occurs where σ_ρ drops below 5 kg m^{-3} and does
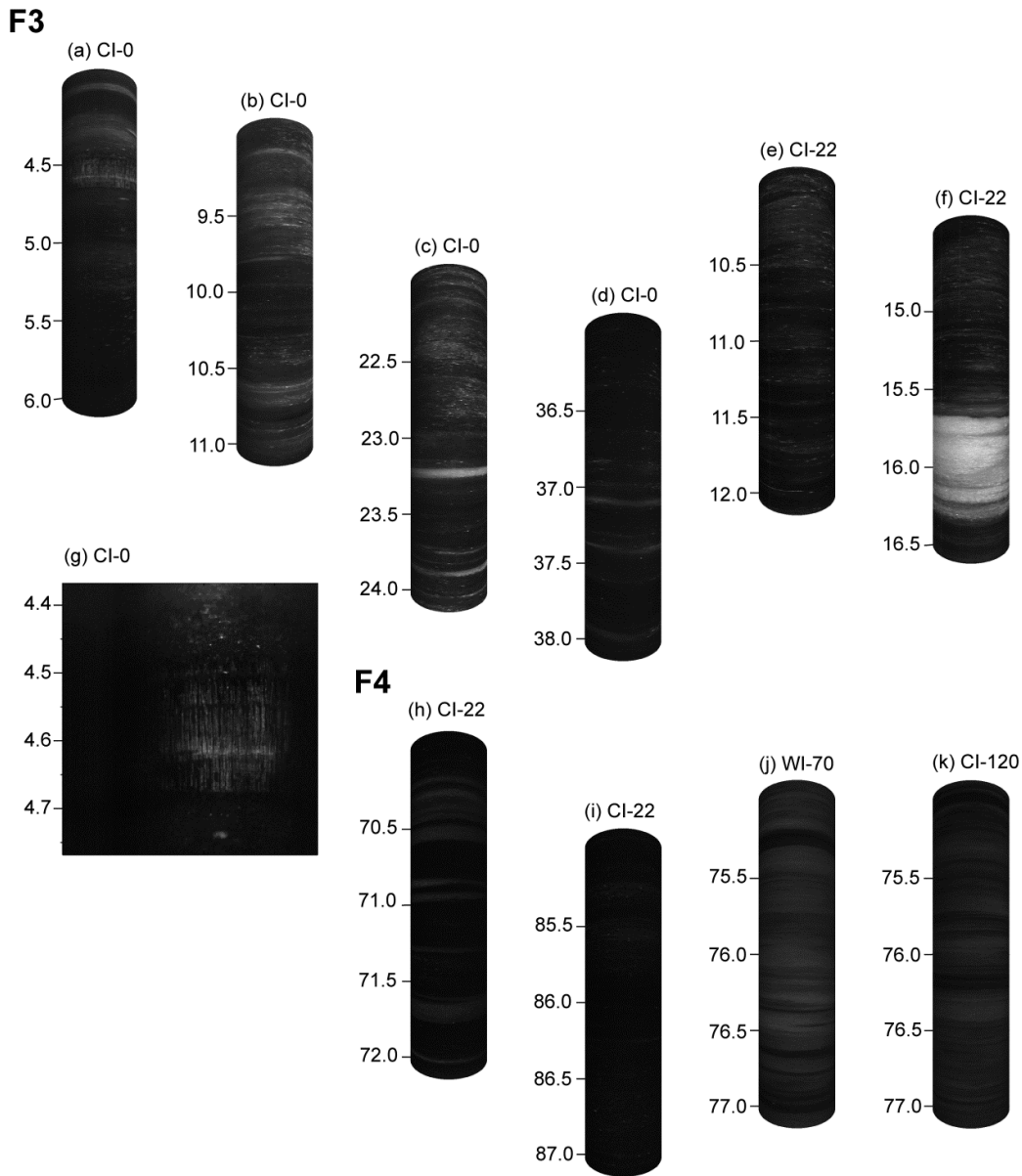
318   not exceed it for the remainder of the log.

319

Figure 6. Rolled virtual core images of LCIS borehole OPTV logs arranged by depth (not to scale) of F3 and F4 with actual depth given in metres.

F5 is characterised by an increase in brightness with depth, yielding an equivalent decrease in luminosity-derived density in this facies (Table 3). F5 is present in only in the two landward sites (CI-0 and WI-0), located closest to the mouths of the two inlets (Fig. 1). F5 contains steeply dipping layers (Fig. 7), sporadic decimetre scale thick dark layers (Fig. 7a and 7b) and metre thick sections of undisrupted ice (e.g. Fig 7d). Layers of different styles cut across one

327   another, as shown in Fig. 7a and 7f. These dipping layers may have diffuse edges (Fig 7b and

328   7e) or be well defined (Fig 7d). Layers and features are not exclusively (quasi-) planar, for

329   example in CI-0 (Fig. 7b) a dipping bright layer beginning at 58 m depth is associated with a

330   lighter region between 57.2 – 57.5 m. In WI-0 (Fig 7e) a brighter layer at ~63.9 m appears to

331   branch resulting in a spur centred at 63.4 m. In both CI-0 and WI-0 F5 extends beyond the

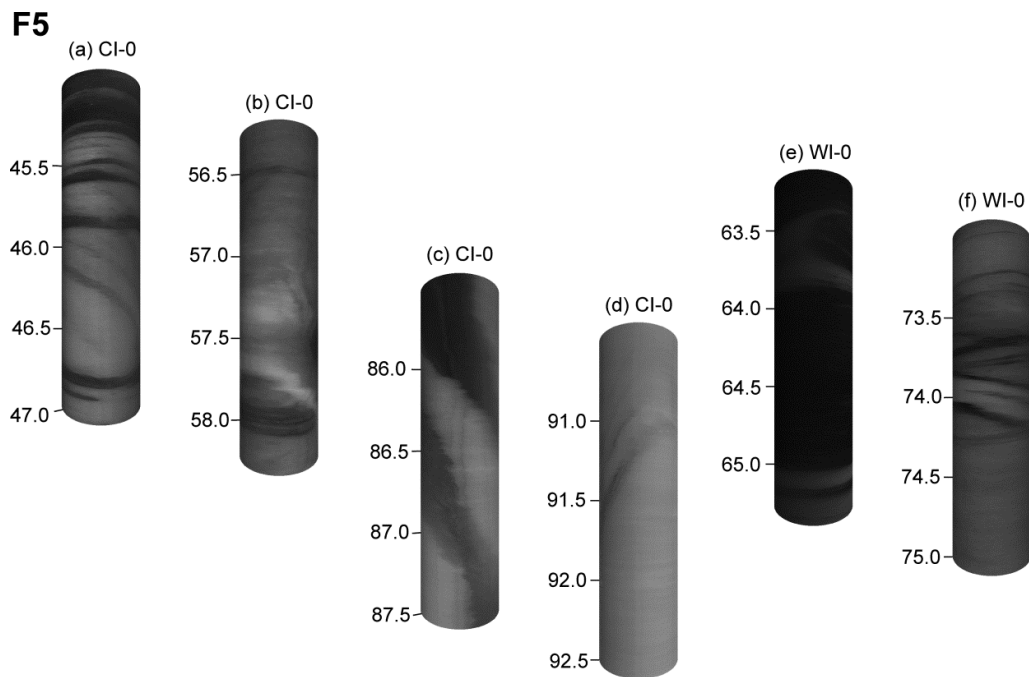332   base of the log and total thickness is unknown (Table 3).

333

334   *Figure 7. Rolled virtual core images of LCIS borehole OPTV logs arranged by depth (not to*

335   *scale) of F5 with actual depth given in metres*

336   *4.3. Image thresholding*

337   Image thresholding results are displayed in Fig. 3 for Cabinet Inlet and Fig. 4 for Whirlwind

338   Inlet, and summarised in Table 3. In those sections where the brighter host material is

339   overlain by darker, low reflectance layers, our thresholding algorithm performs well with

340   identified layers corresponding closely to those identifiable by eye (Fig. 2). However, results

341   become more uncertain in cases of reduced density contrast between melt layers and host ice.

342 Where ice is comprised of a less dense host ice overprinted by dense refrozen ice layers the

343 proportion of ice column comprised by refrozen material is equal to the calculated

344 thresholding output percentage (Table 2). F1 has a thresholding output percentage ranging

345 from 6.5% at CI-0 to 48.6% at CI-120. F2 has a thresholding output percentage ranging from

346 41.0% at CI-120 to 56.4% at CI-22. In F3 the typical host/layer configuration is not present

347 and the thresholding algorithm identifies the absence of speckle clouds and layers, rather than

348 the presence of dark layers, resulting in a thresholding output percentage of 47.7% at CI-0 to

349 66.0% at CI-22. In F4 at CI-120 and WI-70, layers correspond well to visible layers, yielding

350 thresholding output percentages of 41.0% and 56.0% respectively. However, in F4 in the

351 lower part of CI-22 has a thresholding output of 52.2% but its effectiveness is limited by an

352 ice column composed almost exclusively of ice in this zone. F5 has thresholding output

353 percentages of 17.3% at CI-0 and 27.5% at WI-70.

354 *Table 3. Summary of facies, facies density and thresholding output percentage (% Dark)*

355 *results from LCIS borehole OPTV logs. * denotes F3 where assumption of bright background*

356 *and dark layering is not valid. ** denotes that the base of the unit is unknown. Parenthesised*

357 *thickness and firn air contents represent values with the upper 1.87 m (not sampled by OPTV*

358 *log) included.*

Site	Facies	Depth range (m)	% Dark	Mean density ($\pm 1\sigma$) (kgm^{-3})	Firn air (m)	Unit thickness (m)
CI-0	F1	1.87 – 2.90	6.5	696.3 ± 67.0	0.25 (1.12)	1.03 (2.90)
	F3	2.90 – 44.87	47.7*	892.5 ± 7.1	1.12	41.97
	F5	44.87 – 97.50	17.3	852.4 ± 21.0	3.71	52.63**
CI-22	F1	1.87 – 5.90	29.9	822.9 ± 37.4	0.41 (1.08)	4.03 (5.90)
	F3	5.90 – 15.64	66.0*	896.7 ± 5.4	0.22	9.74
	F2	15.64 – 47.61	56.4	889.6 ± 18.3	0.95	31.97
	F4	47.61 – 90.00	52.2	903.8 ± 2.3	0.61	42.39**
CI-120	F1	1.87 – 29.54	48.6	856.6 ± 38.3	1.82 (2.63)	27.67 (29.54)
	F2	29.54 – 68.56	36.5	883.9 ± 9.5	1.41	39.02
	F4	68.56 – 90.00	41.0	899.0 ± 2.1	0.42	21.44**
WI-0	F1	1.87 – 17.34	47.5	825.1 ± 75.2	1.74 (2.52)	15.47 (17.34)
	F2	17.34 – 64.95	55.4	889.5 ± 13.5	1.37	47.61
	F5	64.95 – 90.00	27.5	876.8 ± 7.6	1.10	25.05**
WI-70	F1	1.87 – 32.52	38.8	818.0 ± 67.1	3.31 (4.17)	30.65 (32.52)
	F2	32.52 – 72.48	43.0	880.0 ± 12.2	1.61	39.96
	F4	72.48 – 90.00	56.0	896.1 ± 4.0	0.40	17.52 **

359

360

5. Discussion

5.1. Facies interpretation

The framework for the interpretation of OPTV logs in terms of physical conditions and processes is guided by research indicating LCIS is strongly influenced by föhn winds (Elvidge et al., 2015), which drive intense surface melting and ponding (Holland et al., 2011; Luckman et al., 2014). Föhn-driven melting is focused on the inland portion of the ice shelf, although some melt occurs across almost all LCIS during summer (Luckman et al., 2014; van Wessem et al., 2016). Therefore our interpretative framework is designed to accommodate the OPTV signature of (a) inland-focused, intense, episodic föhn-driven melt and (b) spatially-widespread (but of variable intensity) seasonal melting.

F1 represents snow and firn accumulated on the ice shelf that is progressively undergoing compaction-metamorphism and moderate melt infiltration and refreezing. These processes lead to a facies in which the host ice is densifying and interrupted sporadically by layers of refrozen melt. This observation confirms that substantial melting, meltwater percolation and refreezing on LCIS has been occurring for several decades. The upper 1.87 m is not sampled by the OPTV log and can be safely assumed to also comprise of F1. Thus, F1 has a thickness of 29.54 m at CI-120 and 32.52 m at WI-70. It is relatively thin at CI inland sites (2.90 m at CI-0, 5.90 m at CI-22) as föhn-driven melting and percolation events change the ice character to form either F2 or F3 and prevent the accumulation of a thick F1 layer. F1 at WI-0 is 17.34 m thick, which is thicker than expected given the site's proximity to the grounding line; however, our method based on 2 m σ_ρ may overestimate the true depth of the F1-F2 transition here due to the colder mean annual temperature resulting in less föhn-driven melting. Melt layers are present throughout F1 at all sites, including shelf sites (i.e. CI-120 and WI-70, see Section 2), which, beneath the upper few metres, must be some years or decades old,

385   indicating that the facies is formed by spatially-widespread summer melting, rather than

386   being driven by föhn events restricted to inlet locations.

387   F2 is material that has experienced enhanced firnification due to either föhn-driven melting,

388   not sufficiently intense to form melt ponds (e.g. F2 in CI-22 and see discussion below) or due

389   to climate gradients not directly attributable to föhn events along the flowline. At CI-120 the

390   F1-F2 boundary is unlikely to be directly related to föhn melting as it would have been at the

391   surface downstream of the region thought to be affected by föhn events (Luckman et al.,

392   2014). Van Wessem et al., (2016) discuss the importance of local topography on the

393   meteorology on the eastern Antarctic Peninsula. Therefore the transition to F2 ice may

394   partially reflect the movement of ice away from the influence of topographic features (e.g.

395   Cole Peninsula and Francis Island) and towards open ice shelf conditions. Regardless of the

396   precise mechanism, this warming drives increased compaction rates and meltwater

397   production, which is then available for percolation and refreezing. Despite the dense host ice,

398   refrozen layers are visible throughout F2 and appear to be successfully identified by our

399   thresholding algorithm. There is a potential for equifinality as F1 may densify towards

400   material with an F2-like appearance and there is unlikely to be a clear spatial limit of föhn

401   melting or on the effect of local topographic features. Nevertheless, the step-change in

402   host/layer density contrast at the F1/F2 transition at CI-120 and WI-70 increases our

403   confidence that these are indeed distinct ice facies.

404   Our analysis of the OPTV properties of F3 is consistent with its interpretation as "pond ice"

405   (Hubbard et al., 2016) formed proximal to the location of maximum föhn warming. Here

406   meltwater is abundant enough to refreeze into near-continuous units of massive ice and the

407   meltwater may manifest as surface melt ponds prior to refreezing. The exact mechanism of

408   F3 formation must allow water in the snowpack to become sufficiently mobile to percolate to

409   the previous F1/F3 interface. In this way F3 is built up episodically after periods of extreme

410   melt. Our interpretation of F3 being formed by a significant volume of mobile liquid water is

411   bolstered by features visible in the log. For example, at CI-0 at 4.6 m (Fig. 6a and 6g) a

412   quasi-vertical bright streaking feature is observed. This is interpreted as being formed by an

413   upper and lower freezing-front rejecting dissolved gases and forming two coalescing vertical

414   bubble-trains. The bright speckles that are present throughout F3 are interpreted as bubble

415   clouds. Typically these bubbles form into layers and vary in prominence, as seen in CI-0 22-

416   24m (Fig. 6c), this contrasts within firn layers within F4, as visible in Fig. 6c at the base of

417   F4 in CI-22.

418   F4 is comprised of ice which has undergone enhanced densification in the past but the density

419   contrast between host ice and melt layers is now noticeably diminished. This may be due to

420   in-situ compression of F2 ice as it is buried or represent a change in surface conditions, the

421   manifestation of which is subsequently advected and progressively buried. Consequently, this

422   transition may be abrupt where a change in surface conditions is rapid in either time or space,

423   or gradual where surface conditions change slowly spatially or in cases where the transition

424   reflects the vertical compaction-metamorphism of F2. Furthermore, F4 can be comprised of

425   metamorphosed F2 or F3, such that the transition is more likely to be abrupt where it

426   underlies F3 or less abrupt where it underlies the more variable but generally less dense F2.

427   The transition into F4 is the most subjective of our facies boundaries, and we have therefore

428   attempted to identify it quantitatively as the point at which σ_ρ drops below 5 kg m^{-3} and does

429   not exceed it for the remainder of the log (Section 4.2). In CI-120 this corresponds to a clear

430   visible boundary, which we are confident in attributing to a real facies boundary. In CI-22

431   and WI-70, however, we are less confident of the precise boundary.

432   F5 is ice formed upstream of the region of föhn-driven melting at an inland location of

433   sufficient elevation to experience reduced surface melt intensity. Since F3 ice is interpreted to

434   form though melt pond refreezing, the surface outcrop of the boundary between F3 and F5

435   likely corresponds broadly with the grounding line. This interpretation is supported by the

436   presence of steeply dipping layers up to several metres thick and of variable brightnesses,

437   which we interpret as healed crevasses and other layers having experienced ductile

438   deformation as ice passes over the grounding line. These features are more abundant in CI-0

439   than WI-0 due to the configuration of feeder glaciers in CI leading to a more compressive

440   regime than in WI (Fig. 1). F5 is potentially comparable to the "continental ice" reported by

441   Craven et al. (2005) within Amery Ice shelf. Similar to Amery, this unit, discounting its

442   contorted layers, is bubble-rich and less dense relative to the overlying facies.

443   *5.2. Spatial variability of firn air content and refrozen ice*

444   The pattern of firn air distribution estimated from our OPTV logging (Table 2) is broadly

445   consistent with the pattern identified by Holland et al. (2011). Their results indicate an

446   increase in firn air from 3.0 m at CI-0, to 6.5 m at CI-22, to 10.2 m at WI-0, to 10.6 at CI-120

447   and 12.0 m at WI-70. One notable exception to this spatial correspondence is CI-0, where F5

448   leads to an estimated firn air content in the upper 90 m of 5.18 m. Our results indicate a

449   significant proportion of firn air content is contained within continental ice (F5), an effect

450   that is neglected by commonly applied models of ice shelf firn air content in which firn air

451   thickness is contained within the uppermost densifying layers. Firn air within F5 is an

452   important component of firn air at inlet sites at least. However, the extent and along-flow

453   geometrical development of F5 is unknown. The fact that our firn air estimates (Table 2) are

454   generally lower than those reported by Holland et al. (2011) may indicate that significant firn

455   air is contained at other sites within F5 ice but is not sampled by our borehole logs. Craven et

456   al. (2005) reported on a 205 m thick layer of "white bubbly" continental ice located < 100 km

457   from the ice front at 70 m depth on Amery Ice Shelf directly above a marine ice unit.

458   Independent estimates of full-depth firn air (Nicholls et al., 2012) in LCIS are in agreement

459   with those of Holland et al. (2011). Interpreting OPTV-derived density estimates in terms of

460   firn air places reliance on the luminosity–density relationship of Hubbard et al. (2016). At

461   high densities the RMSE of this relationship is 21.7 kg m^{-3}, an uncertainty which can

462   contribute several metres of firn air over the ice thickness. Despite the uncertainties relating

463   to the absolute density our results indicate that a substantial proportion of firn air is contained

464   at depth, at least at CI-0, within "continental ice" and trapped between refrozen layers at

465   other sites.

466   At each drill site we measured the ice thickness at using a 50 MHz radar, a propagation

467   velocity of 0.166 m ns^{-1} and a firn-velocity correction from a coincident common-offset

468   survey. If the mean densities of F5 at CI-0 and WI-0 extended throughout the remainder of

469   the ice column then 29.2 m and 14.2 m of firn air could be added to the CI-0 and WI-0 values

470   reported in Table 3. At the remaining sites, where F5 is not observed (but may be present at

471   depth in some form) the mean density in the bottom metre (89 – 90 m) is 901 ± 3 kg m^{-3}. If

472   we assume this density extends to the base of the ice shelf at each site then a further firn air

473   content of 6.9 m to CI-22, 3.1 m to CI-120 and 3.5 m to WI-70 would be added. However, we

474   acknowledge that these are maximum estimates as further compression will occur and that

475   the ice-ocean interface will likely be poorly consolidated in areas of basal accretion where

476   some of the "firn air" is taken up by the penetration of relatively dense sea water, although

477   we do not believe any of our sites overlie accreting areas.

478   To estimate the percentage of our OPTV logs composed of refrozen ice from our thresholding

479   output we scale and sum our percentages from each facies according to their depth range. We

480   assume that F3 ("pond ice") and F4 ice in CI-22 both have a thresholding output percentage

481   of 100%. This is justified because F3 pond ice is effectively a specific type of refrozen ice

482   (Hubbard et al., 2016) and we have previously interpreted CI-22 F4 as advected, massive F3

483   ice due to its lack of visible structure. F4 ice in CI-120 and WI-70 maintains its structure and

484   therefore we interpret thresholding output are as the reflecting refrozen ice percentage. A

485   further consideration is that, as the ice column densifies, the vertical velocity will be

486   preferentially accounted for by the compaction of bubble-rich host ice, not the bubble-poor

487   refrozen ice layers. Consequently, it is expected that refrozen ice will constitute a

488   progressively larger proportion deeper in the ice column given constant levels of melt

489   through time. In the absence of further data, we assign the upper 1.87 m, not sampled by

490   OPTV, a thresholding output percentage equal to that of the underlying F1 facies. For 0–90 m

491   depth this results in refrozen ice estimates of 56.5% for CI-0, 79.9% for CI-22, 41.5% for CI-

492   120, 46.1% for WI-0 and 44.0% for CI-70.

493   Those inlet sites most affected by föhn warming (CI-0 and CI-22) have notably higher

494   refrozen ice contents than those less affected by intense föhn warming (WI-0, WI-70, and CI-

495   120). The similar refrozen ice contents of the latter three suggest that these reflect the effect

496   of ice shelf wide seasonal warming, melting and percolation, rather than föhn-driven melting.

497   The relatively low refrozen content of WI-0 may contrast with the conceptual framework of

498   föhn-driven and seasonal melting combining to overprint on the ice column of LCIS.

499   However, we note that the WI-0 refrozen ice content is inclusive of F5 which has a relative

500   paucity of refrozen ice layers (17.3 %, Table 3). F1 and F2 ice at this site therefore accounts

501   for a larger proportion of the total refrozen ice content here.

502   **6.   Conclusion**

503   Herein, we have analysed a suite of five optical televiewer (OPTV) logs from Larsen C Ice

504   Shelf, Antarctica of its northern and central portions. We have reconstructed ice shelf density

505   based on OPTV image luminosity and the refrozen melt portion with a thresholding-based

506   technique. The thresholding technique performs well when the ice column is composed of

507   densifying, reflective host ice which has been overprinted by layers of refrozen melt, but less

508   well where ice is homogenous due to compression or the refreezing of melt ponds. Refrozen

509 ice and remnant refrozen ice makes up >40% of the top 90 m of LCIS and thus is a major

510 contributor to the ice shelf mass redistribution. At inland sites, close to the location of

511 maximum föhn-warming, refrozen ice comprises up to 80% of the top 90 m of the ice

512 column.

513 We bring these observations together to devise a five-part facies scheme defining: F1 as

514 densifying ice shelf accumulation; F2 as föhn-affected densified ice; F3 as ice formed by the

515 refreezing of föhn-driven surface melt ponds; F4 as buried and compressed föhn-affected ice

516 and F5 as lower density continental ice formed upstream of the föhn warming region. While

517 the boundaries between some of these facies are subjective we have taken care to define then

518 in a reproducible, quantitative manner. Where a firn air correction is guided by a firn

519 densification model outputs it neglects the effect of lower density, buried ice from continental

520 sources which may form a significant proportion of the total firn air content at some sites. For

521 example, in Cabinet Inlet (CI-0), the lower unit of continental F5 ice contains 62% of the firn

522 air between 0 and 97.5 m depth, despite occupying the lower 46 % of this depth range. Away

523 from CI-0 the refreezing of melt water effectively traps firn air at depth and this effect should

524 be integrated into firn densifications models used in correcting altimetric data which

525 otherwise risk underestimating the amount of firn air within the ice column. However, if

526 lateral discontinuities in these melt layers can be exploited then this pore space becomes

527 available to be filled by percolating meltwater.

528 This work demonstrates the efficacy of hot-water drilling and OPTV borehole logging in

529 acquiring high-resolution structural and melt information from ice shelves. OPTV logging

530 has successfully imaged bubble structures formed during melt water refreezing, generations

531 of layers which cut across one another formed during ice deformation and fracture close to

532 the grounding line and refrozen ice layers preserved at depths of up to 90 m. The facies

533 scheme outlined here could be extended in the future to include other ice shelf ice types such

534   as dry, cold deposited snow, marine ice or rift ice. Importantly, a growing library of ice

535   OPTV images exists (e.g. Hubbard et al., 2012; Hubbard and Malone, 2013) and could be

536   used to build a unified and widely-applicable facies scheme.

537   **Acknowledgements and Data**

543   **References**

544   1. Banwell, A.F., MacAyeal, D.R. and Sergienko, O.V. (2013) Breakup of the Larsen B
545   Ice Shelf triggered by chain reaction drainage of supraglacial lakes. Geophysical
546   Research Letters, v. 40, p.5872-5876. doi:10.1002/2013GL057694.

547   2. Cape, M. R., Vernet, M., Skvarca, P., Marinsek, S., Scambos, T. and Domack, E.
548   (2015) Foehn winds link climate-driven warming to ice shelf evolution in Antarctica.
549   Journal of Geophysical research: Atmospheres, 120, 11037-11057. doi:
550   doi:10.1002/2015JD023465.

551   3. Chuter, S. J., and J. L. Bamber (2015), Antarctic ice shelf thickness from CryoSat-2
552   radar altimetry. Geophysical Research Letters, 42, 10,721–10,729,
553   doi:10.1002/2015GL066515.

554   4. Cook, A.J. and Vaughan, D.G. (2010) Overview of areal changes of the ice shelves on
555   the Antarctic Peninsula over the past 50 years. The Cryosphere.4:77-98.
556   doi:10.5194/tc-4-77-2010

557   5. Craven, M., Carsey, F., Behar, A., Matthews, J., Brand, R., Elcheikh, A., Hall, S. and
558   Treverrow, A. (2005) Borehole imagery of meteoric and marine ice layers in the
559   Amery Ice Shelf, East Antarctica. Journal of Glaciology, 51 (172), 75-84.
560   doi:10.3189/172756505781829511

6. De Rydt, J., G. H. Gudmundsson, H. Rott, and J. L. Bamber (2015), Modeling the instantaneous response of glaciers after the collapse of the Larsen B Ice Shelf, Geophysical Research Letters, 42, 5355–5363, doi:10.1002/2015GL064355.

7. Drews, R., Brown, J., Matsuoka, K., Witrant, E., Philippe, M., Hubbard, B., and Pattyn, F. (2016) Constraining variable density of ice shelves using wide-angle radar measurements, The Cryosphere, 10, 811-823, doi:10.5194/tc-10-811-2016

8. Elvidge, A. D., Renfrew, I. A., King, J. C., Orr, A., Lachlan-Cope, T. A., Weeks, M. and Gray, S. L. (2015), Foehn jets over the Larsen C Ice Shelf, Antarctica. Quarterly Journal of the Royal Meteorological Society, 141: 698–713. doi: 10.1002/qj.2382

9. Fretwell, P., Pritchard, H. D., Vaughan, D. G., Bamber, J. L., Barrand, N. E., Bell, R., Bianchi, C., Bingham, R. G., Blankenship, D. D., Casassa, G., Catania, G., Callens, D., Conway, H., Cook, A. J., Corr, H. F. J., Damaske, D., Damm, V., Ferraccioli, F., Forsberg, R., Fujita, S., Gim, Y., Gogineni, P., Griggs, J. A., Hindmarsh, R. C. A., Holmlund, P., Holt, J. W., Jacobel, R. W., Jenkins, A., Jokat, W., Jordan, T., King, E. C., Kohler, J., Krabill, W., Riger-Kusk, M., Langley, K. A., Leitchenkov, G., Leuschen, C., Luyendyk, B. P., Matsuoka, K., Mouginot, J., Nitsche, F. O., Nogi, Y., Nost, O. A., Popov, S. V., Rignot, E., Rippin, D. M., Rivera, A., Roberts, J., Ross, N., Siegert, M. J., Smith, A. M., Steinhage, D., Studinger, M., Sun, B., Tinto, B. K., Welch, B. C., Wilson, D., Young, D. A., Xiangbin, C., and Zirizzotti, A.(2013) Bedmap2: improved ice bed, surface and thickness datasets for Antarctica, The Cryosphere, 7, 375-393. doi:10.5194/tc-7-375-2013

10. Glasser, N. F., Holt, T., Fleming, E., and Stevenson, C. (2014) Ice shelf history determined from deformation styles in surface debris. Antarctic Science, 26, 661-673. doi:10.1017/S0954102014000376.

11. Glasser, N.F., Kulessa, B., Luckman, A., Jansen, D., King, E.C., Sammonds, P.R., Scambos, T.A. and Jezek, K.C. (2009) Surface structure and stability of the Larsen C ice shelf, Antarctic Peninsula. Journal of Glaciology, 55, 191, 400-410. Doi: 10.3189/002214309788816597

12. Holland P. R., Brisbourne, A., Corr, H. F. J., McGrath, D., Purdon, K., Paden, J., Fricker, H. A., Paolo, F. S. and Fleming, A. H. (2015) Oceanic and atmospheric forcing of Larsen C Ice-Shelf thinning. The Cryosphere, 9, 1005-1024. Doi: 10.5194/tc-9-1005-2015

593   13. Holland, P. R., H. F. J. Corr, H. D. Pritchard, D. G. Vaughan, R. J. Arthern, A.
594   Jenkins, and M. Tedesco (2011) The air content of Larsen Ice Shelf, Geophysical
595   Research Letters, 38, L10503, doi:10.1029/2011GL047245.

596   14. Hubbard, B. and Malone, T. (2013) Optical-televiewer-based logging of the
597   uppermost 630 m of the NEEM deep ice borehole, Greenland. Annals of Glaciology
598   54, 64, 83-89. 10.3189/2013AoG64A201

599   15. Hubbard, B., Luckman, A., Ashmore, D.W., Bevan, S., Kulessa, B., Kuipers
600   Munneke, P., Philippe, M., Jansen, D., Booth, A., Sevestre, H., Tison, J.-L., O'Leary,
601   M. and Rutt, I. (2016) Massive subsurface ice formed by refreezing of ice-shelf melt
602   ponds, Nature Communications. 7:11897. doi: 10.1038/ncomms11897

603   16. Hubbard, B., Roberson S., Samyn, D. and Merton-Lyn, D. (2008) Digital optical
604   televiewing of ice boreholes. Journal of Glaciology, 54, 188, 823-830.
605   10.3189/002214308787779988

606   17. Hubbard, B., Tison, J., Pattyn, F., Dierckx, M., Boereboom, T. and Samyn, D. 2012.
607   Optical-televiewer-based identification and characterization of material facies
608   associated with an Antarctic ice-shelf rift. Annals of Glaciology 53 (60), 137-146.
609   10.3189/2012AoG60A045

610   18. Hubbard, B., Tison, J., Philippe, M., Heene, B., Pattyn, F., Malone, T. and Freitag, J.
611   2013. Ice shelf density reconstructed from optical televiewer borehole logging.
612   Geophysical Research Letters 40 (22), 5882-5887. 10.1002/2013GL058023

613   19. Hudleston, P.J. (2015) Structures and fabrics in glacial ice: A review. Journal of
614   Structural Geology 81, 1-27. doi:10.1016/j.jsg.2015.09.003

615   20. Jansen, D., Luckman, A. J., Cook, A., Bevan, S., Kulessa, B., Hubbard, B., and
616   Holland, P. R.: Brief Communication: Newly developing rift in Larsen C Ice Shelf
617   presents significant risk to stability, The Cryosphere, 9, 1223-1227, doi:10.5194/tc-9-
618   1223-2015, 2015.

619   21. Kinnard, C., R. M. Koerner, C. M. Zdanowicz, D. A. Fisher, J. Zheng, M. J. Sharp, L.
620   Nicholson, and B. Lauriol (2008), Stratigraphic analysis of an ice core from the Prince
621   of Wales Icefield, Ellesmere Island, Arctic Canada, using digital image analysis:
622   High-resolution density, past summer warmth reconstruction, and melt effect on ice
623   core solid conductivity, Journal of Geophysical Research, 113, D24120,
624   doi:10.1029/2008JD011083.

625   22. Kittler, J. and Illingsworth, J. (1986) Minimum error thresholding, Pattern
626   Recognition, 19, 1, 41-47, doi:10.1016/0031-3203(86)90030-0

627   23. Kuipers Munneke, P., Ligtenberg, S. R.M., van den Broeke, M. R. and Vaughan, D.
628   G. (2014) Firn air depletion as a precursor of Antarctic ice-shelf collapse. Journal of
629   Glaciology, 60 (220). 205-214. 10.3189/2014JoG13J183

630   24. Kulessa, B. Jansen, D., Luckman, A.J., King, E.C. and Sammonds, P.R. (2014)
631   Marine ice regulates the future stability of a large Antarctic ice shelf. Nature
632   Communications. 5: 3707 doi:10.1038/ncomms4707

633   25. Luckman, A., Elvidge, A., Jansen, D., Kulessa, B., Kuipers Munneke, P. King, J. and
634   Barrand, N.E. (2014). Surface melt and ponding on Larsen C Ice Shelf and the impact
635   of föhn winds. Antarctic Science, 26, 625-635. doi:10.1017/S0954102014000339.

636   26. Machguth, H., MacFerrin, M., van As, D., Box, J. E., Charalampidis, C., Colgan, W.,
637   Fausto, R. S., Meijer, H. A. J., Mosley-Thompson, E. and van de Wal, R. S. W.
638   (2016) Greenland meltwater storage in firn limited by near-surface ice formation.
639   Nature Climate Change, 6, 390-393. doi:10.1038/nclimate2899

640   27. Malone, T.S., Hubbard, B.P., Merton-Lyn, D., Worthington, P. and Zwiggelaar, R.
641   (2013) Borehole and Ice Feature Annotation Tool (BIFAT): A program for the
642   automatic and manual annotation of glacier borehole images. Computers and
643   Geosciences 51, 381-389. 10.1016/j.cageo.2012.09.002

644   28. McGrath, D., K. Steffen, H. Rajaram, T. Scambos, W. Abdalati, and E. Rignot (2012),
645   Basal crevasses on the Larsen C Ice Shelf, Antarctica: Implications for meltwater
646   ponding and hydrofracture, Geophysical Research Letters, 39, L16504,
647   doi:10.1029/2012GL052413.

648   29. McGrath, D., K. Steffen, P. R. Holland, T. Scambos, H. Rajaram, W. Abdalati, and E.
649   Rignot (2014), The structure and effect of suture zones in the Larsen C Ice Shelf,
650   Antarctica, Journal of Geophysical Research. Earth Surface, 119, 588–602,
651   doi:10.1002/2013JF002935.

652   30. Morris, E. M. and Vaughan, D. G. (2003) Spatial and Temporal Variation of Surface
653   Temperature on the Antarctic Peninsula And The Limit of Viability of Ice Shelves, in
654   Antarctic Peninsula Climate Variability: Historical and Paleoenvironmental
655   Perspectives (eds E. Domack, A. Levente, A. Burnet, R. Bindschadler, P. Convey and
656   M. Kirby), American Geophysical Union, Washington, D. C.. doi:
657   10.1029/AR079p0061

658   31. Otsu, N. (1979) A threshold selection method from gray-level histograms. IEEE
659   Transactions on systems, man, and cybernetics, 9(1), 62-66. doi:
660   10.1109/TSMC.1979.4310076.

32. Paolo, F. S., Fricker, H.A. and Padman, L. (2015) Volume loss of Antarctic ice shelves is accelerating. Science, March 2015. doi: 10.1126/science.aaa0940

33. Pritchard, H. D., Ligtenberg, S. R. M., Fricker, H.A., Vaughan, D. G., van den Broeke, M. R. and Padman, L. (2012) Antarctic ice-sheet loss driven by basal melting of ice shelves. Nature, 484, 502-505. doi:10.1038/nature10968.

34. Procksch, M., Rutter, N., Fierz, C. and Schneebeli, M. (2016) Intercomparison of snow density measurements: bias, precision, and vertical resolution. The Cryosphere, 10, 371-384. doi:10.5194/tc-10-371-2016.

35. Ridler, T. and Calvard, S. (1978) Picture thresholding using an iterative selection method. IEEE Transactions on systems, man, and cybernetics, 8 (8) (1978), 630–632. doi: 10.1109/TSMC.1978.4310039.

36. Rignot, E., Casassa, G., Gogineni, P., Krabill, W., Rivera, A., Thomas, R. (2004). Accelerated ice discharge from the Antarctic Peninsula following the collapse of Larsen B ice shelf. Geophysical Research Letters, 31 (18), L18401. doi: 10.1029/2004GL020697.

37. Scambos, T. A., Bohlander, J. A., Shuman, C.A. and Skvarca, P. (2004) Glaier acceleration and thinning after ice shelf collapse in the Larsen B embayment. Geophysical Research Letters, 31 L18402. doi: doi:10.1029/2004GL020670,

38. Scambos, T., Fricker, H.A., Liu, C-C., Bohlander, J., Fastook, J., Sargent, A., Massom, R. and Wu, A.M. (2009) Ice shelf disintegration by plate bending and hydro-fracture: Satellite observations and model results of the 2008 Wilkins ice shelf break-ups. Earth and Planetary Science Letters, 280 (1–4), 15, 51–60. doi:10.1016/j.epsl.2008.12.027

39. Scambos, T., Hulbe, C. and Fahnestock, M. (2003) Climate-Induced Ice Shelf Disintegration in the Antarctic Peninsula, in Antarctic Peninsula Climate Variability: Historical and Paleoenvironmental Perspectives (eds E. Domack, A. Levente, A. Burnet, R. Bindschadler, P. Convey and M. Kirby), American Geophysical Union, Washington, D. C.. doi: 10.1029/AR079p0079

40. Turner, J., Lu, H., White, K., King, J. C., Phillips, T., Hosking, J. S., Bracegirdle, T. J., Marshall, G. J., Mulvany, R. and Deb, P. (2016) Absence of 21st century warming on Antarctic Peninsula consistent with natural variability. Nature, 535, 411-41. doi:10.1038/nature18645

41. van Wessem, J. M., Ligtenberg, S. R. M., Reijmer, C. H., van de Berg, W. J., van den Broeke, M. R., Barrand, N. E., Thomas, E. R., Turner, J., Wuite, J., Scambos, T. A.,

695   and van Meijgaard, E.(2016) The modelled surface mass balance of the Antarctic
696   Peninsula at 5.5 km horizontal resolution. The Cryosphere, 10, 271-285,
697   doi:10.5194/tc-10-271-2016